RSC Advances

PAPER

View Article Online
View Journal | View Issue

Cite this: *RSC Adv.*, 2023, **13**, 2248

Albumin-based nanoparticle for dual-modality imaging of the lymphatic system†

Mingze Li, Yundong Zhang, Jinli Ma and Jianshi Du *

The lymphatic system is a complex network of lymphatic vessels, lymph nodes, and lymphoid organs. The current understanding of the basic mechanism and framework of the lymphatic system is relatively limited and not ideal for exploring the function of the lymphatic system, diagnosing lymphatic system diseases, and controlling tumor metastasis. Imaging modalities for evaluating lymphatic system diseases mainly include lymphatic angiography, reactive dye lymphatic angiography, radionuclide lymphatic angiography, computed tomography, and ultrasonography. However, these are insufficient for clinical diagnosis. Some novel imaging methods, such as magnetic resonance imaging, positron emission computed tomography, single-photon emission computed tomography, contrast-enhanced ultrasonography, and near-infrared imaging with agents such as cyanine dyes, can reveal lymphatic system information more accurately and in detail. We fabricated an albumin-based fluorescent probe for dual-modality imaging of the lymphatic system. A near-infrared cyanine dye, IR-780, was absorbed into bovine serum albumin (BSA), which was covalently linked to a molecule of diethylenetriaminepentaacetic acid to chelate gadolinium Gd3+. The fabricated IR-780@BSA@Gd3+ nanocomposite demonstrates strong fluorescence and high near-infrared absorption and can be used as a T1 contrast agent for magnetic resonance imaging. *In vivo* dual-modality fluorescence and magnetic resonance imaging showed that IR-780@BSA@Gd3+ rapidly returned to the heart through the lymphatic circulation after it was injected into the toe webs of mice, facilitating good lymphatic imaging. The successful fabrication of the new IR-780@BSA@Gd3+ nanocomposite will facilitate the study of the mechanism and morphological structure of the lymphatic system.

Received 22nd November 2022
Accepted 27th December 2022

DOI: 10.1039/d2ra07414a

rsc.li/rsc-advances

1. Introduction

The lymphatic system is a complex network system composed of lymphatic vessels, lymph nodes, and lymphoid organs.[1–4] Diseases that cause abnormalities of the lymphatic system are mainly categorized into primary and secondary. Primary diseases include hereditary diseases, lymphoid hypoplasia, lymphoid hypoplasia, and lymphoid hyperplasia.[5,6] Secondary diseases include infectious diseases, traumatic diseases, and malignant tumors.[7–10] Abnormalities of the lymphatic system often lead to the obstruction of tissue fluid return, which leads to tissue edema and reduces the quality of life of patients. Therefore, early detection of lymphatic lesions is particularly important. The methods of visualization of the lymphatic system *in vivo* mainly include direct and indirect injections. Methods that involve direct injections include lymphangiography. Methods that involve indirect injections, also known as intra-tissue injections, mainly include sentinel lymph node (SLN) imaging, radionuclide lymphatic imaging, magnetic resonance imaging (MRI), and near-infrared (NIR) imaging.[11,12] For a long time, lymphography was mainly used to visualize the lymphatic vessels of the lymphatic system. However, it is difficult to perform. It also requires long-term training and may cause vascular infection and lymphedema. It is not used any longer.[13] There are three main options for improvement. Improved tomographic imaging modalities, such as computed tomography (CT) or MRI, are gradually replacing traditional lymphangiography for evaluating lymphatic system lesions. Their advantage is that they can allow clear visualization of the tissue anatomy of the lymphatic system.[14] However, it is difficult for even senior radiologists to distinguish the difference between the lesion and the surrounding tissue due to the characteristics of CT and MRI and the anatomical characteristics of the lymphatic system, and this may easily lead to a missed diagnosis. Intraoperative sentinel lymph node tracing is useful for the diagnosis and treatment of secondary lymphatic system lesions and malignant tumors. However, normal tissue staining can easily occur, resulting in blurring of the surgical field of vision and an increase in the difficulty of surgery.[15] Therefore, it has not been effectively promoted and is mostly used in scientific research. With the development of

Jilin Provincial Key Laboratory of Lymphatic Surgical Disease, Engineering Laboratory of Lymphatic Surgery Jilin Province, China-Japan Union Hospital of Jilin University, Changchun, Jilin, 130031, P. R. China. E-mail: dujs@jlu.edu.cn

† Electronic supplementary information (ESI) available. See DOI: https://doi.org/10.1039/d2ra07414a

functional imaging, more agents, such as 18 F-FDG, 11C-acetate acid, and 11C-methionine, have been developed, and they facilitate the accurate detection of tumor-involved lymph nodes.[16–18] However, tracer imaging does not meet clinical requirements, its biological toxicity and metabolism have not been established, and it cannot be used clinically. Therefore, a safe and effective lymphatic tracing system is urgently needed.

NIR-II imaging involves the detection by an external fluorescence detector of emitted NIR light with a wavelength between 1000 and 1700 nm excited by a fluorescent substance to obtain an image.[19] Indocyanine green (ICG) fluorescence imaging is a new method for SLN imaging developed in recent years.[20,21] As an FDA-approved drug, the fluorescence emitted by ICG can penetrate deep tissues and be detected *in vitro* for accurate localization of the body surface and improved accuracy of lesion detection.[22] Photons are hardly absorbed by the body tissue, and the resulting background fluorescence signal of tissues is typically very low, which prevents the problems of surface localization defects of dyes or radionuclides, complicated procedures, and radioactive contamination. ICG fluorescence imaging is a recently developed method of SLN imaging. After intradermal, subcutaneous, or peritumoral injection of ICG, lymphatic drainage can be rapid and tracked in real time. The half-life of ICG is 2–4 minutes.[23] It is mainly combined with serum albumin and α-1 lipoprotein in the blood,[24] and it is metabolized by the liver. Approximately 90% of ICG is cleared from the blood system within 20 minutes. In general, ICG has relatively few adverse reactions and high detection efficiency and sensitivity and can be used to detect lymphatic vessels and lymph nodes before, during, or after surgery without the side effects of ionizing radiation. Several studies have shown that ICG-guided SLN biopsy has the advantages of a high detection rate, low false negative rate, rapid development, and image clarity.[25–27] However, its penetrating ability is limited, and deep lymph nodes usually affect the concentration of local fluorescent substances. Therefore, a dye with strong penetration and fluorescent signal can compensate for the limitations of ICG. NIR fluorescent dyes have strong emission characteristics and limited autofluorescence in aqueous solvents.[28–30] The most common NIR fluorescent dyes are polymethine cyanine dyes, including pentamethine cyanine and heptamethine cyanine.[31–33] Their extinction coefficients are very high (up to 150 000–250 000 L (mol^{-1} cm^{-1})), and they can be detected in deep tissues under the action of excitation light but cannot be observed with the naked eye. IR-780 is a fluorescent dye that has been studied more recently and will be the focus of our research.[34–36]

Transverse tomography is non-invasive and facilitates rapid examination. On MRI, normal lymph nodes are usually less than 1 cm in size, with smooth and clear boundaries and uniform internal signal and density, and are generally oval or elongated. Given the detectable changes in lymph node size and morphology, MRI is often used for preoperative diagnosis.[37–39] Several studies also use enhanced MRI scans to identify normal and abnormal lymph nodes by the characteristics of lymphatic vessels, such as flow characteristics, blood flow volume, microvascular infiltration, and changes in extracellular volume.[40,41] The application of lymph node contrast agents overcomes the insufficiency of tomographic imaging. Ultrasmall superparamagnetic iron oxide is a newer MRI enhancer that is mainly used for lymph node MR angiography.[42,43] However, only static anatomical features rather than dynamic functional observations are used when assessing whether lymph nodes are involved.

We comprehensively considered the respective characteristics of NIR-II imaging and MRI and developed a novel albumin-based complex for multimodal imaging. In our developed complex, bovine serum albumin (BSA) is conjugated with diethylenetriaminepentaacetic acid (DTPA), which chelates Gd3+ ions and covalently binds to IR-780. The prepared IR-780@BSA@Gd3+ complex demonstrates high fluorescence at an excitation of 600 nm and strong absorption at approximately 808 nm and can be used as a contrast agent for T1-weighted MRI. Apart from facilitating lymphatic tracing, it has a stronger fluorescent signal and improves penetration to facilitate clear visualization of the deep lymphatic system. Meanwhile, NIR-II imaging can be used to dynamically observe the lymph node of the lesion, and the complex has no ionizing radiation, which protects the operator.

2. Experiment

2.1 Materials and reagents

IR-780 was purchased from Sigma-Aldrich. ICG (modified) for human injection was purchased from Dandong Yichuang Pharmaceutical Co. Ltd PBS(phosphate buffer saline) was purchased from HyClone. Gd3+ was purchased from Aladdin. BSA was purchased from Sigma-Aldrich. FBS was purchased from Neuromics. Sucrose was purchased from Sigma-Aldrich.

2.2 Apparatus and measurements

The morphology and structure of IR-780@BSA@Gd3+ were characterized by transmission electron microscopy using a FEI Tecnai F20 transmission electron microscope after staining with phosphotungstic acid (1 wt%). Fluorescence spectra of different samples were obtained on a FluoroMax 4 luminescence spectrometer (HORIBA Jobin Yvon). UV-vis-NIR absorbance spectra were recorded by using a PerkinElmer Lambda 750 UV-vis-NIR spectrophotometer. The dynamic diameter of HSA-Gd3+-IR825 was determined by a Zetasizer Nano-ZS (Malvern Instruments, UK). The concentration of Gd3þ in the HSA-Gd-IR825 sample was measured using inductively coupled plasma atomic emission spectroscopy. IR-780@BSA@Gd3+ solutions with different Gd3þ concentrations ranging from 3.125–50 mM were scanned using a 3.0 T clinical MR scanner (GE Healthcare, USA) at room temperature. After acquiring the T1-weighted MR images, the signal intensity of each sample was measured by drawing regions of interest. By plotting the r_1 value (1/T1) for each sample against the Gd concentration, the final r_1 value for IR-780@BSA@Gd3+ was determined by curve fitting.

2.3 Preparation of IR-780@BSA@Gd3+

P-SCN-Bn-DTPA (2 mg) was dissolved in 200 μL of DMSO to obtain solution A. BSA (20 mg) was dissolved in ddH_2O to obtain

solution B with a concentration of 10 mg mL^{-1}. A and B were mixed according to P-SCN-Bn-DTPA : BAS = 10 : 1 to obtain solution C. It was placed on an ika shaker at 400 rpm and reacted at room temperature for 24 hours. Subsequently, excess P-SCN-Bn-DTPA was removed with an ultrafiltration tube, and 2 ml of ddH_2O was added to obtain a DTPA-BSA solution. The antagonistic solution was PBS.

Gadolinium chloride (2.3 mg) was dissolved in 1000 μL ddH_2O to obtain solution D. Solution D was added dropwise to the DTPA-BSA solution. This was placed on an ika shaker at 400 rpm and reacted at room temperature for 24 hours. At the end of the reaction, excess gadolinium chloride was removed with a 30k ultrafiltration tube to obtain a BSA@Gd3+ solution.

IR780 (13.34 mg) was dissolved in 1 ml of DMSO to obtain a concentration is 20 mmol L^{-1} of solution F. Five microliters of solution F was pipetted into solution BSA@Gd3+ and reacted at 50 °C on a shaker at 214 rpm for 2 h to obtain IR 780@BSA@Gd3+.

2.4 Characterization

Fluorescence spectra of different samples were obtained on a FluoroMax 4 luminescence spectrometer (HORIBA Jobin Yvon). UV-vis-NIR absorbance spectra were recorded by using a PerkinElmer Lambda 750 UV-vis-NIR spectrophotometer.The concentration of Gd3þ in the HSA-Gd-IR825 sample was measured using inductively coupled plasma atomic emission spectroscopy. IR-780@BSA@Gd3+ solutions with different Gd3þ concentrations ranging from 3.125 mM to 50 mM were scanned using a 3.0 T clinical MR scanner (GE Healthcare, USA) at room temperature. After acquiring the T1-weighted MR images, the signal intensity of each sample was measured after drawing regions of interest. By plotting the r_1 value (1/T1) for each sample against the Gd concentration, the final r_1 value for IR-780@BSA@Gd3+ was determined by curve fitting.

3. Results and discussion

3.1 General characteristics of complexes containing IR-780

To observe the brightness of different dyes and complexes in natural light and the NIR-II region, we synthesized three complexes. A schematic diagram of the complex preparation process is provided in Scheme 1. As shown in Fig. 1a, different complexes and dyes exhibit different colors under natural light. On examining the performance of different complexes and dyes in the NIR-II region (Fig. 1b) under the conditions of 808 nm laser irradiation and 3.0 ms exposure duration, IR-780@BSA was the brightest and ICG@BSA was the darkest; free IR-780 and free ICG hardly develop. To further explore the interaction between dyes and BSA, protein gel electrophoresis was used to detect the bands of different dyes and complexes. We found that IR-780@BSA with IR-780 chelated, BSA@ Gd3+ with chelated Gd, and IR-780@BSA@ Gd3+ with IR-780 and Gd3+ chelated in the same band position as BSA (Fig. 1c), indicating that IR-780 and Gd did not change the protein properties of BSA. NIR-II imaging showed that the band positions of IR-780@BSA and IR-780@BSA@Gd3+ (Fig. 1d) were consistent

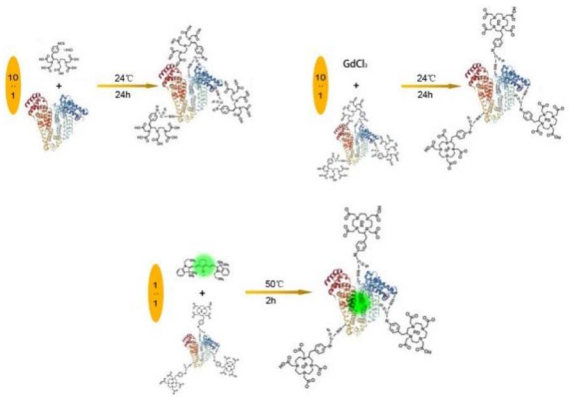

Scheme 1

with those of BSA (Fig. 1c), indicating that IR-780 and Gd were not free. Instead, it is chelated on BSA and exists stably in a complex state. To further observe the durability of different composites, we obtained the durability curve. As shown in Fig. 1e, the dye complexes chelated with BSA demonstrated stronger NIR-II fluorescence than IR-780 and ICG in the free state. Furthermore, the complexes chelated with BSA demonstrated good fluorescence stability over time. The intensity of IR-780@BSA@Gd3+ gradually decreased after 60 min; however, the double-dominance compensated for the deficiency. The reason for the appearance of a similar normal distribution curve is that the rare earth element Gd has seven positive charges on the surface; its chelation with BSA does not affect its surface charge and it maintains its usefulness for excellent NMR (Nuclear magnetic resonance) imaging. After being irradiated by an 808 nm laser, the seven positive charges on the surface of Gd were activated, and the brightness gradually increased during NIR-II development. At the same time, the surface charge of Gd destroyed BSA, and it gradually decayed after the NIR-II brightness reached a peak. As shown in Fig. 1e, the small

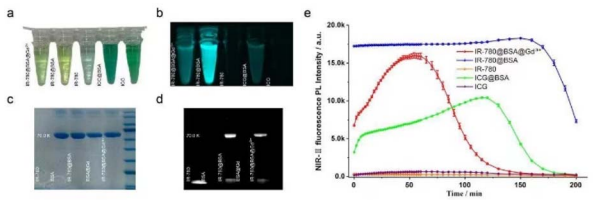

Fig. 1 General states of different complexes. (a) Color performance of different dyes and complexes at the same concentration under natural light (from left to right: IR-780@BSA@Gd3+; IR-780@BSA; IR-780; ICG@BSA; ICG). (b) Brightness performance of different dyes and complexes at the same concentration in the near-infrared II region (NIR-II) (from left to right: IR-780@BSA@Gd3+; IR-780@BSA; IR-780; ICG@BSA; ICG). (c) Protein gel electrophoresis to observe the band positions of different dyes and complexes. (d) NIR-II imaging of protein gels to observe the band positions of different dyes and complexes. (e) The fluorescence intensity decay curves of different substances over time (red: IR-780@BSA@Gd3+; blue: IR-780@BSA; orange: IR-780; green: ICG@BSA; purple: ICG).

ICG molecule and IR-780 cause fluorescence quenching due to the effect of the water solvent, resulting in a weak fluorescence for NIR-II. ICG@BSA and IR-780@BSA demonstrated strong NIR-II fluorescence emission, which indicates that the combination with BSA can prevent the fluorescence extraction of ICG and IR780.

3.2 MRI representation of complexes containing IR-780 and Gd3+

To observe the development of bimodal complexes using MRI, we prepared free Gd and IR-780@BSA@ Gd3+ of different concentrations. As shown in Fig. 2a, the MR signal gradually increased with the increase of the Gd concentration. In addition, the same MR images showed the same concentrations of Gd and IR-780@BSA@Gd3+, suggesting that Gd can chelate to BSA and exist stably and play the same developing role. Fig. 2b suggests that the concentration and brightness slopes of IR-780@BSA@Gd3+ are similar to that of free Gd, which proves that IR-780@BSA@Gd3+ stably chelates Gd and is useful for MR imaging.

3.3 Excellent visualization of IR-780@BSA@Gd under MRI and NIR-II

To determine the complex in the lymphatic system *in vivo*, we observed the expression of NIR-II in C57BL/6 mice after injections of different complexes. After the injections of IR-780@BSA@Gd3+ (left) and free IR-780 (right) in the toe webs of both lower limbs of mice under the condition of 808 nm excitation light, imaging of the lower limb lymphatic vessels of NIR-II mice at different time points was performed. As shown in Fig. 3a and d, both IR-780@BSA@Gd3+ and free IR-780 entered and developed into lymphatic vessels. Compared with free IR-780, IR-780@BSA@Gd3+ can be imaged using NIR, and the imaging is better than that of free IR-780. This provides effective support for the diagnosis of clinical lymphatic system diseases. The usefulness of NIR-II after the injections of IR-780@BSA@Gd3+ and IR-780@BSA was determined in the same way. As shown in Fig. 3b and e, IR-780@BSA@Gd3+ demonstrated the same developing effect as IR-780@BSA over time. This differs from the results of the *in vitro* in-tube experiments (Fig. 1e) and fully illustrates the biostability of the complexes. To further observe the systemic distribution of the complex after injection, IR-780@BSA@Gd3+ was injected into the toe webs of mice. As shown in Fig. 3c and f, IR-780@BSA@Gd3+ was mainly concentrated in the draining lymph nodes after it was

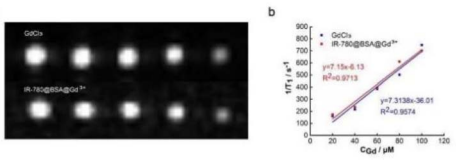

Fig. 2 MR imaging of free Gd and IR-780@BSA@Gd3+. (a) MR imaging of free Gd (upper column) and IR-780@BSA@Gd3+ (lower column) at different concentrations. (b) Concentration (Gd)-signal intensity (T1) curve.

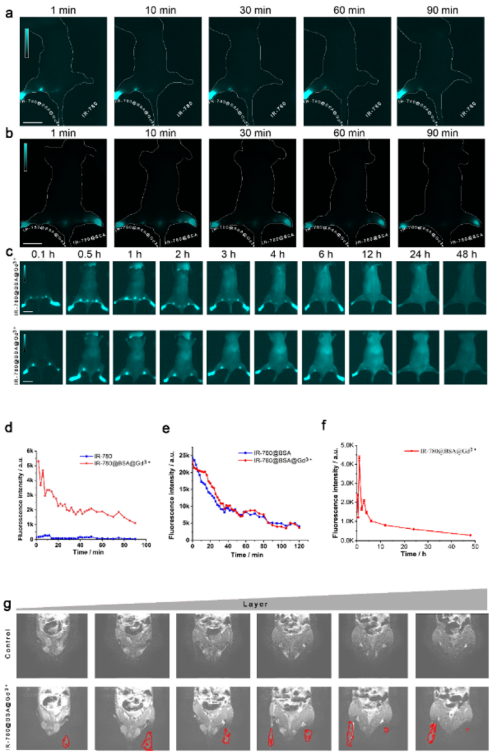

Fig. 3 Evaluation of the usefulness of bimodal complexes for MRI and NIR-II and the difference between different dyes and complexes for NIR-II imaging. (a) NIR-II at different times under 808 nm light excitation after the injection of different substances to the left and right lower limb webs of mice (left: IR-780@BSA@Gd3+, right: free IR-780) (b). NIR-II at different times under 808 nm light excitation after the injection of different substances on the left and right lower limb webs of mice (left: IR-780@BSA@Gd3+ right: IR-780@BSA). (c) NIR-II at different times under light excitation of 808 nm after the injection of IR-780@BSA@Gd3+ to the toe webs of the bilateral lower limbs of mice (upper: dorsal view, lower: ventral view). (d) Quantitative line graph for the brightness of Fig. 3a. (e) Quantitative line graph for the brightness of Fig. 3b. (f) Quantitative line graph for the brightness of Fig. 3c. (g) Sagittal image of T1 fat reduction after IR-780@BSA@Gd3+injection to the bilateral toe webs of C57BL/6 male mice obtained with MRI.

injected into the lymphatic system and distributed throughout the body. Over time, the complex was still enriched in the lymph node at the twelfth hour, suggesting that IR-780@BSA@Gd3+ has good stability and can be enriched and it stably existed in the lymphatic system. To further ascertain the lymphatic tracing ability of IR-780@BSA@Gd3+, MR imaging was observed after the injection of the complex. As shown in Fig. 3g, the lymphatic system can be visualized in mice by MRI (red dotted line) after the injection of IR-780@BSA@Gd3+ (lower) compared with no injection of IR-780@BSA@Gd3+ (upper).

3.4 IR-780@BSA@Gd3+has the advantages of early imaging, easy metabolism, and less accumulation *in vivo*

To evaluate the metabolic changes of different complexes and dyes in mice, NIR-II imaging was performed with tail vein injection. As shown in Fig. 4a, the development of mice at

different time points (0.1 h, 0.5 h, 1 h, 2 h, 3 h, 4 h, 6 h, 12 h, 24 h, 48 h, 72 h, 96 h) was observed after IR-780@BSA@Gd3+ IR-780@BSA and free IR-780 were injected into the tail vein. Over time, IR-780@BSA@Gd3+ had similar metabolic rates and metabolic pathways as IR-780@BSA. The distribution peaked at 24 h after administration. Conversely, free IR-780 was imaged later and metabolized slower than IR-780@BSA. In conclusion, IR-780@BSA@Gd3+ facilitates early imaging and easy metabolism and is less accumulated in the body. IR780@BSA can show a better fluorescence within 0.1–24 hours and facilitate rapid metabolism; however, fluorescence can rarely be observed at 96 h. However, the effect of single IR-780 fluorescence imaging is weak, and there is still fluorescence at the ninety-sixth hour, indicating that metabolism is slow. To further observe the enrichment of various tissues and organs after tail vein injection of different compounds, they were sacrificed and observed using NIR-II imaging. As shown in Fig. 4b, both IR-780@BSA@Gd3+and IR-780@BSA can be metabolized *in vivo* for 24 h, which does not easily lead to the accumulation of complexes and reduce the toxic and side effects. On the contrary, free IR-780 accumulates in the lungs, and IR-780 in the free state should not be used in clinical practice due to its deposition in organs and toxic and side effects. To quantify the changes in the fluorescence intensity of the three substances with time, we developed a fluorescence intensity-time quantitative line chart. As shown in Fig. 4c, the fluorescence intensity of IR-780@BSA was better than those of IR-780@BSA@Gd3+ and free IR-780. Over time, the fluorescence intensity of IR-780@BSA@Gd3+ decreased more rapidly than that of IR-780@BSA. In Fig. 4d and b, three substances are less distributed in the spleen and intestine and more distributed in the lung and liver, suggesting that the complex is metabolized by the liver and lung.

3.5 Lymphatic system of IR-780@BSA@Gd3+ tracer lesions under MRI and NIR-II

To further verify the excellent tracing effect of IR-780@BSA@Gd3+ in the edematous lymphatic system, we successfully prepared lymphedema model mice. As shown in Fig. 5a, the lymphatic fluorescence imaging after the injection of IR-780@BSA@Gd3+ to the toe webs of the lower limbs of the lymphedema model mice in different positions was observed in the NIR-II area. IR-780@BSA@Gd3+can be developed during NIR-II and nuclear MR imaging. In addition, IR-780@BSA@Gd3+ only enters the lymphatic system, and the interference of surrounding tissues is removed; the imaging of the lymphatic system is more precise and intuitive, and it can dynamically observe whether the edema lymphatic vessels are blocked. MRI was used to observe the edema of the lower limbs of the lymphedema model mice, as shown in Fig. 5b and c; green shows edema lesions captured with MRI without IR-780@BSA@Gd3+ injection, and red represents the edema

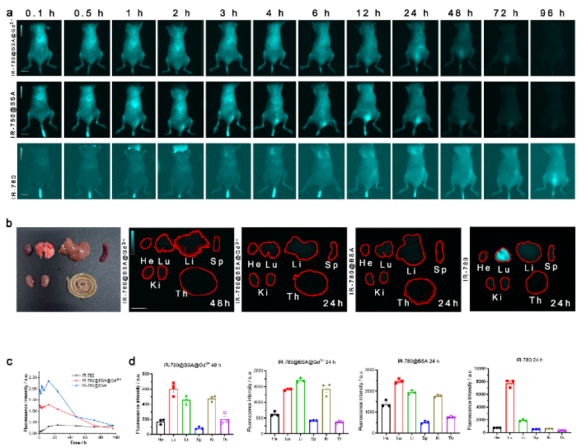

Fig. 4 Evaluation of metabolic changes in different complexes in mice. (a). NIR-II images at different times with 808 nm light excitation after injections of different substances into the tail vein of mice (top: IR-780@BSA@Gd3+; middle: IR-780@BSA, bottom: free IR-780). (b) NIR-II imaging results of various tissues and organs under 808 nm light excitation light at different time points after mice were injected with different substances in the tail vein (from left to right:IR-780@BSA@Gd3+ 48 h; IR-780@BSA@Gd3+ 24 h; IR-780@BSA 24 h; free IR-780 24 h). (c) Quantitative broken line statistics of epidermal fluorescence intensity changes with time after mice were injected with different substances in the tail vein. (d) Quantitative analysis of the fluorescence intensity in the near-infrared region II of each tissue and organ at different time points after injections of different substances into the tail vein of mice (from left to right: IR-780@BSA@Gd3+ 48 h; IR-780@BSA@Gd3+ 24 h; IR-780@BSA 24 h; Free IR-780 24 h).

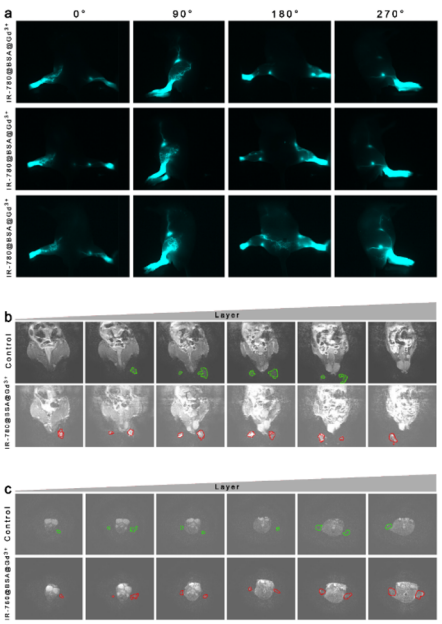

Fig. 5 Lymphatic imaging of the bimodal complexes in lymphedema model mice. (a) NIR-II imaging of lymphedema model mice after injection of IR-780@BSA@Gd3+ into the toe webs of both lower limbs. (b) Sagittal T1 fat reduction image after injection of IR-780@BSA@Gd3+in the toe webs of both lower limbs of lymphedema model mice (green: edema lesions without complex injection, red: edema lesions after complex injection). (c) Axial image of T1 fat reduction after injection of IR-780@BSA@Gd3+ in the toe webs of both lower limbs of lymphedema model mice (green: edema lesions without complex injection, red: edema lesions after complex injection).

lesions imaged after the injection of the IR-780@BSA@Gd3+ using MRI. At the same level, no matter the sagittal or axial view, the experimental group could determine the surrounding tissue edema and the lymphatic system edema. In addition, it assisted in judging the anatomical changes and lesions of the surrounding tissue, but the diagnosis and anatomical location of the disease need to be determined by doctors with several years of clinical experience.

4. Conclusion

NMR can only be used to observe tissue structures under static conditions, which often requires diagnosis by senior clinicians, and NIR-II has deep penetration but cannot be used to visualize surrounding tissues. A compound protein developer IR-780@BSA@Gd3+ was synthesized by modifying IR-780 and Gd3+ on BSA, which can be used for NIR-II imaging and nuclear magnetic resonance imaging. IR-780@BSA@Gd3+can not only be used for accurate localization and visualization with NMR; it can also be used to dynamically observe the structural and functional changes in lymphatic vessels using NIR-II. We performed *in vivo* and *in vitro* imaging experiments by combining IR-780, IR-780@BSA, and IR-780@BSA@Gd3+, respectively. We verified that IR-780 and Gd3+ did not change the organizational structure of BSA, and IR-780 and Gd3+ could exist in a complex with BSA. IR-780@BSA@Gd3+ also has a 780 nm NIR function and can be used for Gd3+nuclear magnetic imaging function. In addition, the dye complexes chelated with BSA have similar NMR imaging results and the same NIR-II fluorescence intensity as Gd3+and IR-780 in the free state. We verified the biosafety of IR-780@BSA@Gd3+ *in vitro* and *in vivo*. The complex did not reduce cell proliferation and had no significant effect on mouse organ function. The imaging of IR-780@BSA@Gd3+ in the lymphatic system *in vivo* was significantly better than that of free IR-780, which was distributed in the systemic lymphatic system and mainly concentrated in the draining lymph nodes. IR-780@BSA@Gd3+ has good stability and can enrich and exist stably in the lymphatic system. As a biological dye, IR-780 has an unknown metabolic pathway *in vivo*, while IR-780@BSA@Gd3+ can accelerate the metabolism of IR-780 *in vivo* and reduce biological toxicity. At the same time, IR-780@BSA@Gd3+ facilitates a more precise and intuitive visualization of the lymphatic system and can be used to dynamically observe the edema lymphatic vessels for blockage to assist in judging the anatomical changes and lesions of surrounding tissues. This study suggests a novel approach for diagnosis by clinicians. Our experiments show that IR-780@BSA@Gd3+ has good dual-mode imaging function and is an effective nanomaterial for disease diagnosis. Next, we consider linking corresponding drugs to proteins for the treatment of lymphatic system diseases to produce a dual-mode nanomaterial for the integrated diagnosis and treatment of lymphedema.

Ethical statement

All of the animal experiments were performed following the guidelines of the Animal Care Committee at Jilin University, Changchun, China. All animal studies were conducted in accordance with the principles and procedures outlined in the National Institutes of Health (NIH) Guide for the Care and Use of Laboratory Animals and under protocols approved by the NIH Clinical Center Animal Care and Use Committee (protocol number: NIBIB 16-03).

Conflicts of interest

There are no conflicts to declare.

Acknowledgements

This work was supported by grants from the Changchun Science and Technology Bureau Key R&D Program (21ZY17) and Jilin Province Innovation Capacity Building Program (2019C007).

References

1 S. P. Leong, A. Pissas, M. Scarato, F. Gallon, M. H. Pissas, M. Amore, M. Wu, M. B. Faries and A. W. Lund, The lymphatic system and sentinel lymph nodes: conduit for cancer metastasis, *Clin. Exp. Metastasis*, 2021, **39**(1), 139–157.
2 K. Alitalo, The lymphatic vasculature in disease, *Nat. Med.*, 2011, **17**(11), 1371–1380.
3 P. Baluk, J. Fuxe, H. Hashizume, T. Romano, E. Lashnits, S. Butz, D. Vestweber, M. Corada, C. Molendini, E. Dejana and D. M. McDonald, Functionally specialized junctions between endothelial cells of lymphatic vessels, *J. Exp. Med.*, 2007, **204**(10), 2349–2362.
4 S. Pal, C. J. Meininger and A. A. Gashev, Aged Lymphatic Vessels and Mast Cells in Perilymphatic Tissues, *Int. J. Mol. Sci.*, 2017, **18**(5), 965.
5 P. Brouillard, M. H. Witte, R. P. Erickson, R. J. Damstra, C. Becker, I. Quere and M. Vikkula, Primary lymphoedema, *Nat. Rev. Dis. Primers*, 2021, **7**(1), 77.
6 E. Lee, D. M. Biko, W. Sherk, W. R. Masch, M. Ladino-Torres and P. P. Agarwal, Understanding Lymphatic Anatomy and Abnormalities at Imaging, *Radiographics*, 2022, **42**(2), 487–505.
7 P. Zeppa and I. Cozzolino, Lymphadenitis and Lymphadenopathy, *Monogr. clin. cytol.*, 2018, **23**, 19–33.
8 T. Rudiger and E. Geissinger, Infectious lymphadenitis, *Pathologe*, 2011, **32**(5), 428–435.
9 N. Fujimoto and L. C. Dieterich, Mechanisms and Clinical Significance of Tumor Lymphatic Invasion, *Cells*, 2021, **10**(10), 2585.
10 V. Mumprecht and M. Detmar, Lymphangiogenesis and cancer metastasis, *J. Cell. Mol. Med.*, 2009, **13**(8A), 1405–1416.
11 F. Zhang, G. Niu, G. Lu and X. Chen, Preclinical lymphatic imaging, *Mol. Imaging Biol.*, 2011, **13**(4), 599–612.
12 M. Absinta, S. K. Ha, G. Nair, P. Sati, N. J. Luciano, M. Palisoc, A. Louveau, K. A. Zaghloul, S. Pittaluga, J. Kipnis and D. S. Reich, Human and nonhuman primate

meninges harbor lymphatic vessels that can be visualized noninvasively by MRI, *Elife*, 2017, **6**, e29738.

13 L. Vaillant and V. Tauveron, Primary lymphedema of limbs, *Presse Med.*, 2010, **39**(12), 1279–1286.

14 J. Dinnes, L. Ferrante di Ruffano, Y. Takwoingi, S. T. Cheung, P. Nathan, R. N. Matin, N. Chuchu, S. A. Chan, A. Durack, S. E. Bayliss, A. Gulati, L. Patel, C. Davenport, K. Godfrey, M. Subesinghe, Z. Traill, J. J. Deeks and H. C. Williams, Cochrane Skin Cancer Diagnostic Test Accuracy, G., Ultrasound, CT, MRI, or PET-CT for staging and re-staging of adults with cutaneous melanoma, *Cochrane Database Syst. Rev.*, 2019, **7**, CD012806.

15 N. S. van den Berg, O. R. Brouwer, B. E. Schaafsma, H. M. Matheron, W. M. Klop, A. J. Balm, H. van Tinteren, O. E. Nieweg, F. W. van Leeuwen and R. A. Valdes Olmos, Multimodal Surgical Guidance during Sentinel Node Biopsy for Melanoma: Combined Gamma Tracing and Fluorescence Imaging of the Sentinel Node through Use of the Hybrid Tracer Indocyanine Green-(99m)Tc-Nanocolloid, *Radiology*, 2015, **275**(2), 521–529.

16 R. Guglielmi, G. Andreisek and B. S. Halpern, (18)F FDG imaging - response criteria in tumors, *Eur. J. Radiol.*, 2022, **147**, 110054.

17 L. M. Deford-Watts, A. Mintz and S. J. Kridel, The potential of (1)(1)C-acetate PET for monitoring the Fatty acid synthesis pathway in Tumors, *Curr. Pharm. Biotechnol.*, 2013, **14**(3), 300–312.

18 R. Nakajima, K. Kimura, K. Abe and S. Sakai, (11)C-methionine PET/CT findings in benign brain disease, *Jpn. J. Radiol.*, 2017, **35**(6), 279–288.

19 Y. Su, B. Yu, S. Wang, H. Cong and Y. Shen, NIR-II bioimaging of small organic molecule, *Biomaterials*, 2021, **271**, 120717.

20 J. H. Kim, M. Ku, J. Yang and H. K. Byeon, Recent Developments of ICG-Guided Sentinel Lymph Node Mapping in Oral Cancer, *Diagnostics*, 2021, **11**(5), 891.

21 E. Kaplan-Marans, J. Fulla, N. Tomer, K. Bilal and M. Palese, Indocyanine Green (ICG) in Urologic Surgery, *Urology*, 2019, **132**, 10–17.

22 J. S. Taylor, J. Zeki, N. Ikegaki, L. L. Chen and B. Chiu, Combined application of Indocyanine green (ICG) and laser lead to targeted tumor cell destruction, *J. Pediatr. Surg.*, 2018, **53**(12), 2475–2479.

23 K. Leung, 2-[2-[2-Chloro-3-[2-[1,3-dihydro-3,3-dimethyl-1-(4-sulfobutyl)-2H-indol-2-ylidene]-ethylidene]-1-cyclohexen-1-yl]-ethenyl]-3,3-dimethyl-1-(4-sulfobutyl)-3H-indoli um, in *Molecular Imaging and Contrast Agent Database (MICAD)*, Bethesda (MD), 2004.

24 Y. Oh, Y. H. Quan, Y. Choi, C. K. Kim, H. Kim, H. K. Kim and B. M. Kim, Intraoperative combined color and fluorescent images-based sentinel node mapping in the porcine lung: comparison of indocyanine green with or without albumin premixing, *J. Thorac. Cardiovasc. Surg.*, 2013, **146**(6), 1509–1515.

25 H. Ferreira, A. V. Smith and A. Wattiez, Application of Indocyanine Green in Gynecology: Review of the Literature, *Surg. Technol. Int.*, 2019, **34**, 282–292.

26 H. C. Zeng, J. L. Hu, J. W. Bai and G. J. Zhang, Detection of Sentinel Lymph Nodes with Near-Infrared Imaging in Malignancies, *Mol. Imaging Biol.*, 2019, **21**(2), 219–227.

27 I. Ruscito, M. L. Gasparri, E. I. Braicu, F. Bellati, L. Raio, J. Sehouli, M. D. Mueller, P. B. Panici and A. Papadia, Sentinel Node Mapping in Cervical and Endometrial Cancer: Indocyanine Green *Versus* Other Conventional Dyes-A Meta-Analysis, *Ann. Surg. Oncol.*, 2016, **23**(11), 3749–3756.

28 Y. Sheng, Z. Wang, G. M. Ngandeu Neubi, H. Cheng, C. Zhang, H. Zhang, R. Wang, J. Zhou and Y. Ding, Lipoprotein-inspired penetrating nanoparticles for deep tumor-targeted shuttling of indocyanine green and enhanced photo-theranostics, *Biomater. Sci.*, 2019, **7**(8), 3425–3437.

29 T. Jin, C. Huang, M. Cui, Y. Yang, Z. Wang, W. Zhu and X. Qian, Supramolecular ensembles modified by near-infrared dyes and their biological applications, *J. Mater. Chem. B*, 2020, **8**(47), 10686–10699.

30 M. Asgher, S. A. Qamar, M. Sadaf and H. M. N. Iqbal, Multifunctional materials conjugated with near-infrared fluorescent organic molecules and their targeted cancer bioimaging potentialities, *Biomed. Phys. Eng. Express*, 2020, **6**(1), 012003.

31 Y. Du, X. Liu and S. Zhu, Near-Infrared-II Cyanine/Polymethine Dyes, Current State and Perspective, *Front. Chem.*, 2021, **9**, 718709.

32 A. P. Gorka, R. R. Nani and M. J. Schnermann, Harnessing Cyanine Reactivity for Optical Imaging and Drug Delivery, *Acc. Chem. Res.*, 2018, **51**(12), 3226–3235.

33 N. Lange, W. Szlasa, J. Saczko and A. Chwilkowska, Potential of Cyanine Derived Dyes in Photodynamic Therapy, *Pharmaceutics*, 2021, **13**(6), 818.

34 G. Capistrano, A. A. Sousa-Junior, R. A. Silva, F. Mello-Andrade, E. R. Cintra, S. Santos, A. D. Nunes, R. M. Lima, N. Zufelato, A. S. Oliveira, M. Pereira, C. H. Castro, E. M. Lima, C. G. Cardoso, E. Silveira-Lacerda, S. A. Mendanha and A. F. Bakuzis, IR-780-Albumin-Based Nanocarriers Promote Tumor Regression Not Only from Phototherapy but Also by a Nonirradiation Mechanism, *ACS Biomater. Sci. Eng.*, 2020, **6**(8), 4523–4538.

35 Y. J. Lu, A. T. S, C. C. Chuang and J. P. Chen, Liposomal IR-780 as a Highly Stable Nanotheranostic Agent for Improved Photothermal/Photodynamic Therapy of Brain Tumors by Convection-Enhanced Delivery, *Cancers*, 2021, **13**(15), 3690.

36 M. Luo, L. Chen, J. Zheng, Q. Wang, Y. Huang, F. Liao, Z. Jiang, C. Zhang, G. Shen, J. Wu, Y. Wang, Y. Wang, Y. Leng, S. Han, A. Zhang, Z. Wang and C. Shi, Mitigation of radiation-induced pulmonary fibrosis by small-molecule dye IR-780, *Free Radical Biol. Med.*, 2021, **164**, 417–428.

37 R. M. Mann, N. Cho and L. Moy, Breast MRI: State of the Art, *Radiology*, 2019, **292**(3), 520–536.

38 Y. Zhang and J. Yu, The role of MRI in the diagnosis and treatment of gastric cancer, *Diagn. Interv. Imaging*, 2020, **26**(3), 176–182.

39 S. Kijima, T. Sasaki, K. Nagata, K. Utano, A. T. Lefor and H. Sugimoto, Preoperative evaluation of colorectal cancer

using CT colonography, MRI, and PET/CT, *World J. Gastroenterol.*, 2014, **20**(45), 16964–16975.

40 B. Huang, D. L. Kwong, V. Lai, Q. Chan, B. Whitcher and P. L. Khong, Dynamic Contrast-Enhanced Magnetic Resonance Imaging of Regional Nodal Metastasis in Nasopharyngeal Carcinoma: Correlation with Nodal Staging, *Contrast Media Mol. Imaging*, 2017, **2017**, 4519653.

41 S. Gaddikeri, R. S. Gaddikeri, T. Tailor and Y. Anzai, Dynamic Contrast-Enhanced MR Imaging in Head and Neck Cancer: Techniques and Clinical Applications, *AJNR Am. J. Neuroradiol.*, 2016, **37**(4), 588–595.

42 H. C. Thoeny, S. Barbieri, J. M. Froehlich, B. Turkbey and P. L. Choyke, Functional and Targeted Lymph Node Imaging in Prostate Cancer: Current Status and Future Challenges, *Radiology*, 2017, **285**(3), 728–743.

43 H. E. Daldrup-Link, Ten Things You Might Not Know about Iron Oxide Nanoparticles, *Radiology*, 2017, **284**(3), 616–629.